RSC Advances

PAPER

View Article Online
View Journal | View Issue

Cite this: *RSC Adv.*, 2015, **5**, 43279

Mesocarbon microsphere composites with Fe_3O_4 nanoparticles for outstanding electromagnetic interference shielding effectiveness

Ridham Dhawan,[a] Saroj Kumari,*[a] Rajeev Kumar,[a] S. K. Dhawan[b] and Sanjay R. Dhakate[a]

Received 23rd February 2015
Accepted 28th April 2015

DOI: 10.1039/c5ra03332b

www.rsc.org/advances

Development of advanced carbon based materials with improved microstructure properties, finding widespread applications in electromagnetic shielding is a challenge for the scientific community. This research paper describes a method, which is simple and economic for the synthesis of mesocarbon microspheres (MCMS) from heat treatment of coal tar pitch and petroleum pitch followed by solvent extraction. The MCMS were then semi-graphitized (GMCMS) at 1400 °C and the distance between the graphitic layers of GMCMS was increased by a chemical treatment called expanded EMCMS. Further, Fe_3O_4 nanoparticles were *in situ* incorporated in GMCMS and EMCMS. All the samples were characterized for various parameters, particularly with regard to their potential use in electromagnetic interference shielding effectiveness in the X-band of the frequency range of 8.2 GHz to 12.4 GHz. A maximum total shielding effectiveness (SE_T) of −65.4 and −75.8 dB for GMCMS–Fe_3O_4 and EMCMS–Fe_3O_4, respectively was achieved which is more than double for the bare samples, *i.e.*, −29 and −32 dB for GMCMS and EMCMS, respectively. A total SE_T was obtained for the EMCMS–Fe_3O_4 composite of ∼−75.8 dB in the whole X band which is remarkably high compared to other reported values in the literature. EM parameters such as relative complex permittivity and relative complex permeability of all the composites were also studied in the X band frequency range.

1. Introduction

Electromagnetic interference (EMI) shielding is an undesired electromagnetic (EM) induction triggered by extensive use of telecommunication frameworks, cellular phones, high-speed communication frameworks, military gadgets and wireless devices, *etc.*[1] Due to the increased demand of high operational frequency and bandwidth in electronic frameworks, there are increased chances and risks of deterioration of the radio-wave environment, which is known as EMI.[2] This EMI has unfavourable consequences for electronic supplies, for example, false operation because of unwanted electromagnetic waves and spillage of data in remote telecommunications. Thus, in order to maintain electromagnetic similarity of the finished product, lightweight EMI shielding materials are needed to maintain a healthy working environment for electronic gadgets.[3] Thus, the absorption or reflection of electromagnetic radiations by a material, which then acts as a shield for the penetration of radiation (*e.g.* radio waves from our mobile devices interfere with electronics like computer), is called Electromagnetic Interference (EMI) shielding.[4] The rapid growth of radio frequency sources and the increase in society's demand for reliable electronics have increased the importance of EMI shielding in today's world. EMI shielding both of radio wave and microwave frequencies have been in great demand for communication technology.[5–7]

In past few decades much attention is being paid towards the synthesis of advanced EM wave absorbing materials for military and civil applications, like stealth technology or the reduction in radar signals of ships, aircrafts and tanks, in order to make an aircraft partially invisible to detection on radar.[8] An ideal microwave absorber is a special material that can effectively absorb electromagnetic waves with reduce backscattering from material.

Traditionally, metal and metal composites due to their high electrical conductivity and shielding effectiveness were used as shielders for electromagnetic waves. Although they are great for EMI shielding, but they are susceptible to corrosion, oxidation, poor chemical resistance and complex processing methods.[9,10] Thus, carbon based materials have attracted the attention of researchers for their application in EMI shielding due to their chemical inertness, corrosion resistance, thermal stability, high electrical conductivity and high strength.[2,8,11,12]

[a]*Physics & Engineering of Carbon Group, Material Physics and Engineering Division, CSIR-National Physical Laboratory, Dr. K. S. Krishnan Marg, New Delhi-110012, India. E-mail: kumaris@mail.nplindia.org; Tel: +91-11-45608285*

[b]*Polymeric and Soft Materials Group, Material Physics and Engineering Division, CSIR-National Physical Laboratory, Dr. K. S. Krishnan Marg, New Delhi-110012, India*

There are numerous research papers that give an account of EMI shielding of different carbon based material and carbon reinforced polymer composites in the X-band (8.2–12.4 GHz) area due to its utilization in military correspondence satellites, climate forecasting, aviation authority, defense tracking and high-determination imaging radars.[13–15]

Carbon materials, such as graphite flakes, carbon nanotubes (CNTs), graphene, carbon nanofibers, carbon foams, *etc.*[16–22] have been extensively studied as microwave absorber for suppression of EMI. Among the various carbon materials, mesocarbon microspheres (MCMS), a kind of micro-dimension conducting material are not studied for EMI application, although they represent an industry benchmark as anode materials for lithium-ion batteries.[23–25] MCMS are not only highly conducting but also possess high mechanical strength, thermal and chemical stability. Hence, it can contribute to promising shielding applications in severe environments including spacecraft, aircrafts, and shelters along with many other electronic encloses.

However, ideal microwave absorption properties cannot be obtained for MCMS due to their low magnetic loss factor. For large amount of microwave absorption by the shield, it must possess, along with high electrical conductivity, magnetic or electric dipoles, which connects with the electromagnetic fields in the radiations. Materials like Fe_3O_4 particles, which provide the magnetic dipole, have high magnetic permeability that can be achieved by using multilayer magnetic films, which reduce the number of magnetic domain walls. During past few years, Fe_3O_4 nanoparticles have been intensively studied as promising microwave absorption materials owing to their satisfactory magnetic properties, low toxicity, high compatibility, strong spin polarization at room temperature[26–28] and synergetic interaction between dielectric and magnetic absorbers.[29,30] However, low thermal stability and aggregation of Fe_3O_4 nanoparticles hamper their wide applications.

Thus, in the present work we have attempted to investigate MCMS as a promising material for EMI shielding. MCMS were prepared from heat treatment of coal tar pitch and in order to obtain uniform spheres with high yield, petroleum pitch was added as an additive and carbon source as well in coal tar pitch prior to heat treatment. Further, MCMS was semi-graphitized by heat treating at 1400 °C in inert atmosphere. The porosity and specific surface area of semi-graphitized MCMS was then enhanced by modified Hummer's method,[31] which overcame the defects and improved the excellent characteristics of MCMS for better EMI application.

Also, we have diversified our research to *in situ* synthesis of MCMS–Fe_3O_4 nanoparticles composites, in order to enhance the absorption of electromagnetic. So far, although good microwave absorption results are being reported, there is no literature regarding the synthesis of MCMS from heat treatment of mixture of coal tar pitch and petroleum pitch, *in situ* incorporation of magnetic nanoparticles (Fe_3O_4) in the matrix of semi-graphitized and expanded MCMS and their composites as a shield material for EMI shielding application. All samples were also characterized for various properties in order to make a relationship between properties of the material with EMI shielding.

2. Experimental

2.1. Material

Coal tar pitch (CTP) and petroleum pitch (PP) were procured from Konark Industry Pvt. Ltd. India. The solvents toluene (99.0%), quinoline (99.0%) and acetone (99.0%) required for extraction of MCMS were purchased from Qualigenes Fine Chemicals, Navi Mumbai, India. The precursor for synthesis of iron oxide nanoparticles, iron(II) sulfate heptahydrate (GR) ($FeSO_4 \cdot 7H_2O$) and solvent ethylene glycol were purchased from Merck, Mumbai, India. The other chemicals sodium hydroxide pellets (GR) which was used as a pH controller and sodium nitrate used as a reducing agent during the preparation of iron oxide nanoparticles were supplied by Merck, India.

2.2. Methods

2.2.1. Preparation of mesocarbon microspheres (MCMS). Coal tar pitch (CTP) and petroleum pitch (PP) with characteristics given in Table 1 were mixed in 1 : 1 ratio and grinded. As seen from Table 1, the quinoline insoluble (QI) content of precursors, *i.e.*, CTP and PP were very low about 0.2–2% which signifies the primary QI which is basically the impurities present in pitch and are responsible for prevention of coalescence of mesophase spherules. The mixture was then transferred into a distillation assembly where the low molecular weight volatiles were removed by the process distillation and also the polymerization of some low molecular mass aromatics which can exhibit mesophase take place simultaneously at 400 °C for about 2 hours. The following heat-treatment facilitates polymerization and condensation reactions among the various molecular species, as well as allows the relatively low molecular weight components of the pitch material/volatiles to escape.

After that, the pitch was then pyrolysed at 370 °C for 6 hours in inert atmosphere of nitrogen to carry out further polymerization and growth of carbon spherules in the pitch, the mixture was then cooled to room temperature and black solid material was obtained. The spherules, *i.e.*, MCMS were then separated from the black solid material by Soxhlet extraction using quinoline and tar oil in 1 : 6 ratio. The extracted MCMB's were washed with toluene and acetone followed by calcination at 320 °C for 2 hours in inert atmosphere. Table 1 demonstrates that the QI content increased to about 96% in MCMS, it is the secondary QI, which is basically the amount of MCMS developed in the pitch as a result of various polymerization and polycondensation reaction during heat treatment. MCMS are insoluble in quinoline as during the process different small

Table 1 Characteristics of coal tar pitch and petroleum pitch

Characteristics	Coal tar pitch	Petroleum pitch	MCMS
Quinoline insoluble (%)	1.05	0.25	96.30
Softening point (°C)	95.50	125	—
Specific gravity	1.32	1.22	1.30
Coking value (%)	46.70	53.6	92.6

aromatic rings aggregate or polymerize to form large molecular weight complex structures which due to their large size do not dissolve in quinoline and thus separated as secondary QI content. The increase in softening point and coking value can also be attributed to removal of low molecular volatiles from the pitch.

MCMS's thus obtained were semi-graphitized by heat-treating at 1400 °C in inert atmosphere of nitrogen to get more crystalline GMCMS. The detailed process for the preparation of MCMS and GMCMS composites is given in Fig. 1.

2.2.2. Preparation of expanded MCMS. In order to obtain expanded MCMS (EMCMS), GMCMS were added to 1 : 2 mixture of concentrated nitric acid and sulfuric acid with constant stirring at 45 °C for 20 minutes. The mixture was then put into an ice bathe maintained at temperature < 15 °C. After that $KMnO_4$ and $FeCl_3$ were respectively added to the above mixture to take part in the intercalation reaction of GMCMS with constant stirring at a slow rate. The reaction was carried out for 2 hours at constant temperature with stirring on magnetic stirrer. The mixture was filtered and washed using de-ionized water and dried at 100–150 °C in an oven to obtain Expanded MCMS (EMCMS) (Fig. 1).

2.2.3. Preparation of MCMS–Fe_3O_4 composites. 0.7 g of ferrous sulfate heptahydrate, 2.5 g of sodium hydroxide (NaOH) and 0.2 g of sodium nitrate ($NaNO_3$) were taken in three separate beakers and dissolved in 7 mL, 20 mL and 30 mL of 1 : 1 ethylene glycol (EG) and de-ionized water solution, respectively. The EG being a high boiling solvent is used for reduction of metal salts and also it stabilizes the growth of nanoparticles preventing their agglomeration. The three solutions were heated to 70 °C and the temperature was maintained constant for 30 minutes. The $NaNO_3$ solution, which acts as an oxidizing agent was then added to $FeSO_4$ solution followed by addition of NaOH solution, a greenish-blue precipitate was formed. To this mixture, 4 g of GMCMS prepared in Section 2.2.1 was added, the mixture was constantly stirred for 2 hours on a magnetic stirrer, and then kept for aging in N_2 atmosphere for a day. After aging pH of the solution was checked, if it was found to be less than 10 then more NaOH solution was added and the mixture was again stirred for 2 hours at 70 °C. The solution was then filtered, washed with distilled water and dried to obtain GMCMS–Fe_3O_4 composite powder. The same process was repeated for expanded MCMS to obtain EMCMS–Fe_3O_4 composites powder. Schematic diagram for the same has been shown in Fig. 1. Powders of GMCMS, EMCMS, GMCMS–Fe_3O_4 and EMCMS–Fe_3O_4 were mixed with 30% of phenolic resin and moulded into rectangular plates of dimension 60 × 20 × 4 mm^3 using hydraulic press and carbonized at 1000 °C in inert atmosphere of nitrogen.

3. Characterization

Surface morphology of the MCMS composite samples was observed by a scanning electron microscope (SEM, VP-EVO, MA-10, Carl-Zeiss, UK) operating at an accelerating potential of 10.0 kV. The crystal structure of the MCMS composite samples was studied by X-ray diffraction (XRD, D-8 Advanced Bruker diffractometer) using CuKα radiation (λ = 1.5418 Å). Raman spectra of the GMCMS and EMCMS samples were recorded using Renishaw Raman spectrometer, UK, with laser as an excitation source at 514 nm. BET surface area was measured by using an autosorbiQ automated gas sorption analyzer from Quantachrome Instruments, USA (model no. ASIQM0000-4 and N_2 adsorption isotherm from Germany).

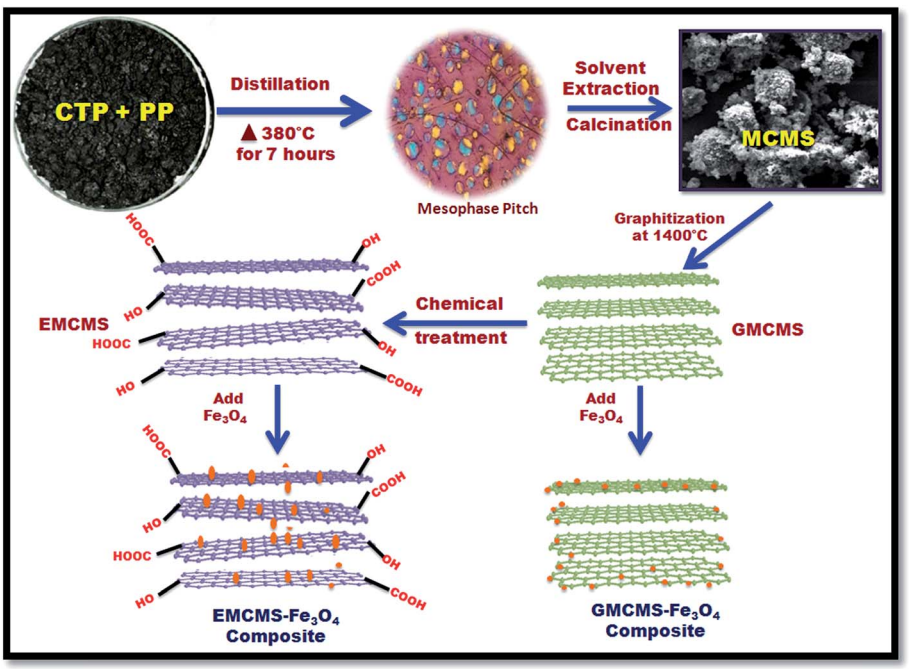

Fig. 1 Schematic of synthesis of MCMS and MCMS–Fe_3O_4 composites.

Transmission electron microscope (TEM) (FEI, Tecnai T30) was used to investigate the crystallite size of Fe_3O_4 nanoparticles. The magnetic property of the MCMS samples was measured by vibration sample magnetometer (VSM) model 7304 (Lakeshore Cryotronics Inc., USA) with a maximum magnetic field of 1.2 T, using a Perspex holder vibrating horizontally at frequency of 76 Hz. Thermal stability and weight percentage of incorporated Fe_3O_4 nanoparticles present in MCMS composite is investigated by thermo gravimetric analyzer (TGA, Mettlar Toledo) in air atmosphere @ 10 °C min^{-1}. The electrical conductivity of samples was measured by DC four probe contact method using a Keithley 2602A programmable current source for providing current. EM-SE and EM attributes (complex permittivity and permeability) were measured by waveguide using vector network analyzer (VNA E8263B Agilent Technologies). The rectangular samples of thickness ~2.5 mm were placed inside the cavity of the sample holder, which matches with the internal dimensions of the X-band (8.2–12.4 GHz) waveguide.

4. Results and discussion

4.1. Analysis of synthesized GMCMS and EMCMS

Fig. 2A and B show the SEM micrographs of GMCMS and EMCMS, respectively. As seen in Fig. 2A graphitized MCMS are of spherical shape with diameter in the range of 10–20 μm. It is interesting to see that EMCMS retained their spherical shape with diameter of ~20 μm even after chemical treatment and it is also clear that the interlayer distance between the graphitic layers of EMCMS was increased and thus cracks were developed on the surface of MCMS that can be clearly seen in Fig. 2B.

The effect of heat treatment followed by expansion of MCMS was further confirmed by XRD studies. XRD spectra of GMCMS and EMCMS are shown in Fig. 2C, curve (a) and (b), respectively. A sharp and narrow peak around 26° in Fig. 2C curve (a) corresponds to, (002) peak of carbon due to proper orientation of graphitic layer whereas in Fig. 2C curve (b) the wide and small peak shows the intercalation and poor orientation of graphitic layer on expansion.

This could be attributed to the fact that on heat treating MCMS at high temperature, the graphitic layers get properly stacked over one another thereby resulting in proper orientation. Whereas on being chemically treated, van der Waals forces between the graphitic layers loose and are held together by free bonding due to which the interlayer distance between the graphitic layers increases and same can be seen in above graph. The interlayer distance, *i.e.*, d_{002} is increased from 0.3504 nm in (a) to 0.3618 nm in (b) of Fig. 2C.

To further confirm the XRD results, Raman analysis on the same samples were carried out. The main features of Raman spectra of carbon material are its D and G-band peaks that lie around 1360 and 1560 cm^{-1}, respectively for the visible excitation. Fig. 2D shows Raman spectra of two different samples of MCMS. The peak at 1360 cm^{-1} Raman shift is for A_{1g} vibrational mode (D-band), which is induced by the defects in carbon samples and its intensity reduces on proper alignment of graphitic sheets inside the sample. Raman shift at 1560 cm^{-1} is for E_{2g} vibration mode (G-band), which is the overtone of D peak but is found only in defect free samples.

The curve (a) in Fig. 2D is Raman spectrum of GMCMS and intensity of D peak is less as compared to G peak. This is due to the reduction in grain boundaries or defect sites in MCMS. When we further expanded the graphitized MCMS, the graphitic layers got intercalated leading to poor orientation that caused

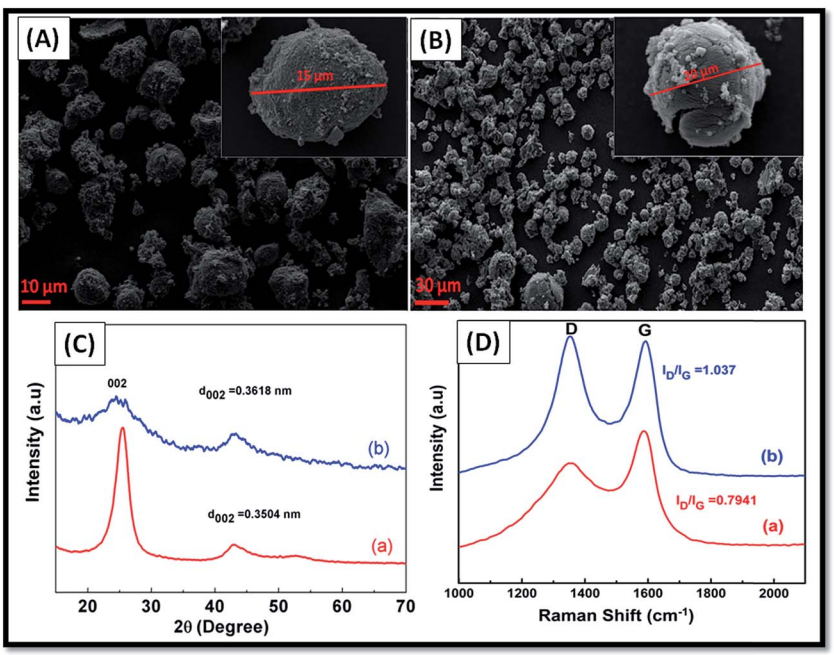

Fig. 2 SEM micrographs of (A) GMCMS and (B) EMCMS; XRD spectra of (C) GMCMS (curve (a)) and EMCMS (curve (b)) and Raman spectra of (D) GMCMS (curve (a)) and EMCMS (curve (b)) (a color version of this figure can be viewed online).

the increase in intensity of D peak thereby reducing the intensity of G peak which is in accordance with the data obtained by XRD analysis of the same sample. As a result, I_D/I_G ratios for each curve were calculated and are found to be 0.7941 and 1.037 for GMCMS and EMCMS, respectively.

BET analyses of the powdered samples confirmed that surface area of EMCMS was improved from 14.79 m^2 g^{-1} in GMCMS to 24.44 m^2 g^{-1} in EMCMS. These results further confirmed that expansion of graphitized MCMS by chemical treatment successfully took place and the results are also in accordance with data obtained by XRD and Raman analysis.

4.2. Analysis of GMCMB and EMCMB composite with Fe_3O_4 nanoparticles

To confirm the structural and morphological properties of Fe_3O_4 nanoparticles, these nanoparticles were also synthesized separately and characterized using XRD and TEM. Fig. 3A shows the XRD pattern of the Fe_3O_4 nanoparticles, which is quite identical to pure magnetite and matched well with JCPDS no. 19-0629, this indicates that the sample has a cubic crystal system.[32,33] Also, there is no characteristic peak due to impurities. The mean crystallite size is 13.4 nm, calculated from the XRD curve according to the line width of the (311) plane refraction peak using Scherrer's equation. Fig. 3B shows the TEM image of Fe_3O_4 nanoparticles, from which we can see that sizes of Fe_3O_4 nanoparticles are almost uniform and most of Fe_3O_4 nanoparticles are approximately spherical in shape with the mean diameters of ~15 nm. The results are in agreement with the results obtained from the XRD analysis. However, the particle diameters observed from TEM measurements are slightly larger than the crystal sizes seen from XRD which is due to the presence of noncrystalline surface layers on particles.[33]

Nanoparticles of iron oxide were then synthesized *in situ* with GMCMS and EMCMS to obtain GMCMS–Fe_3O_4 and EMCMS–Fe_3O_4 composites. Fig. 4A and B show the SEM micrographs of Fe_3O_4 nanoparticles incorporated in GMCMS and EMCMS, respectively. The white particles deposited on the surface of GMCMS correspond to Fe_3O_4 nanoparticles in Fig. 4A which are aggregated to each other whereas in Fig. 4B these particles are present on the surface as well as in between the cracks formed as a result of expansion or intercalation of graphitic layers of GMCMS.

The presence of these nanoparticles was further confirmed by XRD analysis. The peaks of graphitized carbon and Fe_3O_4 nanoparticles are clearly visible in the XRD pattern as shown in Fig. 4C. The peak at 2θ of 26.6° is due to the crystalline (002) phase of carbon in MCMS, whereas other sharp peaks at 2θ value of 30.08, 35.42, 43.06, 53.41, 56.93 and 62.54° correspond to Fe_3O_4 phase of iron oxide with (*hkl*) value of (220), (311), (400), (422), (333) and (440), respectively. Similarly, Fig. 4D shows XRD pattern of EMCMS–Fe_3O_4 composite formed by adding Fe_3O_4 to expanded MCMS. All peaks of Fe_3O_4 nanoparticles with very small carbon peak in EMCMS can be clearly seen in the XRD plot of the composite. This confirms that the composite has characteristics of both the parent materials.

Magnetism properties of GMCMS, GMCMS–Fe_3O_4 and EMCMS–Fe_3O_4 composites are further confirmed by vibrating magnetometer at room temperature and their graphs are presented in Fig. 5A.

The data of magnetization expose that GMCMS does not show any magnetization throughout the magnetic field because carbon is in the high crystalline phase with high electrical conductivity due to delocalized π electron with no magnetic properties. However, plot of as such Fe_3O_4 nanoparticles exhibits superparamagnetic behavior as remanence and coercivity are zero. This is due to the small size of Fe_3O_4 nanoparticles (<20 nm) already earlier confirmed by XRD and TEM analysis; because superparamagnetism phenomena occurs for small magnetic nanoparticles which consist one domain. Whereas, GMCMS–Fe_3O_4 and EMCMS–Fe_3O_4 composites demonstrate narrow hysteresis loop with non zero remanence and coercivity, owing to the fact that Fe_3O_4 nanoparticles get aggregated due to magnetic interaction as confirmed by SEM images (Fig. 4A and B) and surrounded by non-magnetic carbon microspheres in the respective composites, which effects the magnetic properties of bare Fe_3O_4 nanoparticles. The GMCMS–Fe_3O_4 and EMCMS–Fe_3O_4 possess saturation magnetization of 14.37 emu g^{-1} and 33.71 emu g^{-1} at 4900 G, respectively. The higher saturation magnetization in case of EMCMS–Fe_3O_4 is due to the intercalation of graphitic layers in MCMS carbon during expansion. In case of intercalated or

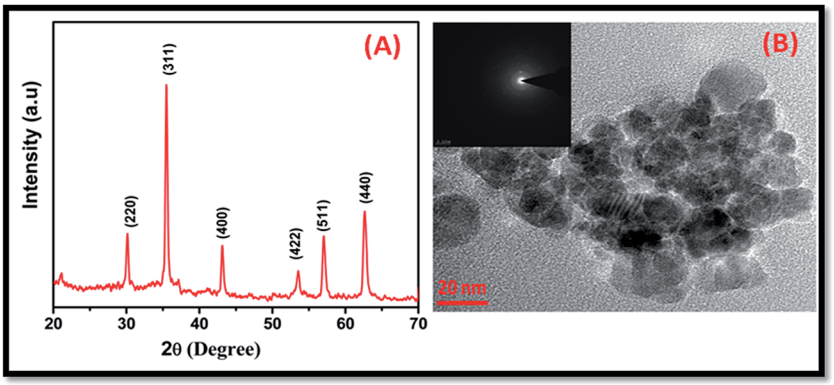

Fig. 3 XRD pattern (A) and TEM image (B) of Fe_3O_4 nanoparticles (a color version of this figure can be viewed online).

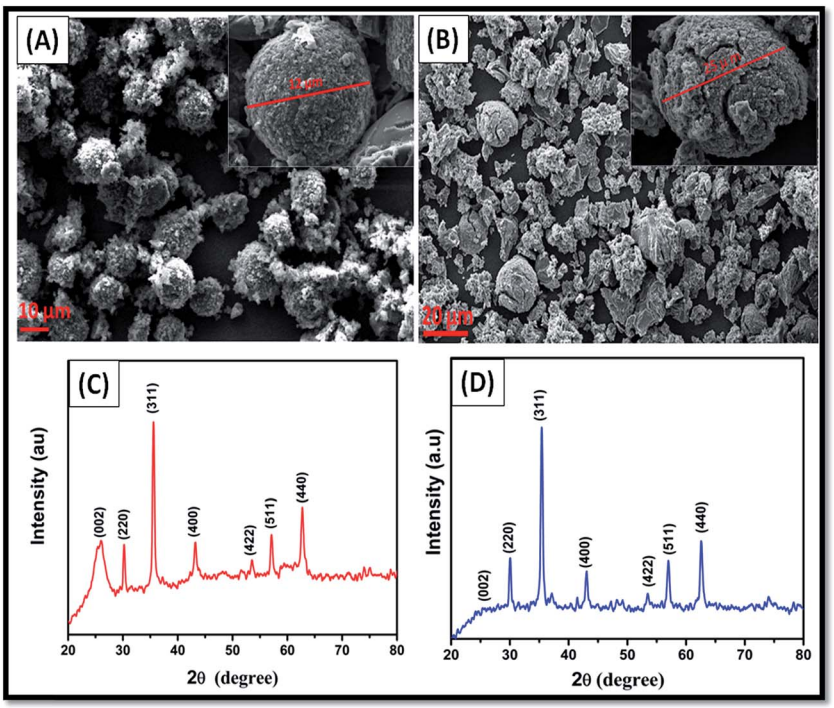

Fig. 4 SEM micrographs of (A) GMCMS–Fe_3O_4 and (B) EMCMS–Fe_3O_4 and XRD spectra of (C) GMCMS–Fe_3O_4 and (D) EMCMS–Fe_3O_4 (a color version of this figure can be viewed online).

expanded MCMS, the Fe_3O_4 nanoparticles easily attached inside the pore or on the surface of MCMS.

Thermal stability of the MCMS composites was investigated by TGA in oxidative (air) atmosphere and is depicted in Fig. 5B. The thermal stability of MCMS depends on arrangement of carbon atoms in the graphitic structure[34] but GMCMS looses it thermal stability on being chemically treated to form EMCMS. This is due to the intercalation of graphitic layers in EMCMS which were properly aligned in GMCMS. It is observed that Fe_3O_4 containing GMCMS and EMCMS composite exhibit higher thermal stability in comparison to GMCMS and EMCMS. The addition of Fe_3O_4 nanoparticles enhances the thermal stability of EMCMS and GMCMS by ~100 °C. In case of GMCMS, weight loss initiated from temperature ~500 °C and total weight loss takes place upto 900 °C, whereas in case of GMCMS and EMCMS composite with Fe_3O_4 weight loss is initiated at 600 °C. In an oxidative environment, weight loss initiation takes place from chemically active site available in GMCMS and EMCMS while in case of GMCMS–Fe_3O_4 and EMCMS–Fe_3O_4 composites, the Fe_3O_4 nanoparticles interact with chemically active sites during the heat treatment, which further enhances the thermal stability of the composites. As seen from Fig. 5B, the GMCMS–Fe_3O_4 composite exhibits better thermal stability in comparison to EMCMS–Fe_3O_4 composite as it has perfectly aligned graphitic layers whereas in EMCMS–Fe_3O_4 composite, intercalated layers held by free bonds reduce it thermal stability in respect to GMCMS–Fe_3O_4 composite. Furthermore, TGA curve also shows that residue left after complete combustion of

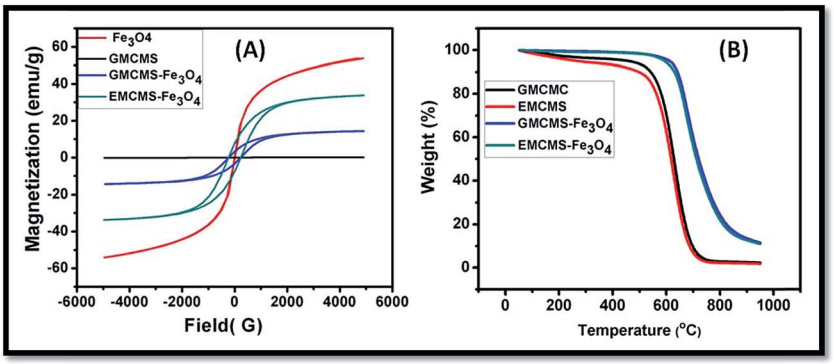

Fig. 5 Magnetization plots (A) and TGA curves (B) of GMCMS, GMCMS–Fe_3O_4 and EMCMS–Fe_3O_4 composites (a color version of this figure can be viewed online).

carbon in oxidative atmosphere at 950 °C was found to be 2.3%, 11.5% and 11.3% in GMCMS, GMCMS–Fe_3O_4 and EMCMS–Fe_3O_4, respectively. From above results it can be inferred that composition of Fe_3O_4 added is 9.2% in GMCMS–Fe_3O_4 composite and 9.0% in EMCMS–Fe_3O_4 composite and rest 2.3% being the ash content or impurities.

4.3. Electromagnetic shielding and microwave absorbing properties of MCMS composites

The MCMS on being heat treated at higher temperature loses its binding properties; therefore in graphitized MCMS and expanded MCMS and their respective composites, about 30% of phenolic resin was added as a binder and hot molded on hydraulic press into plates. The plates thus formed have an insulating layer of non-conducting phenolic resin and thus do not show conductivity. The effect of phenolic resin was nullified by carbonizing the plates at 1000 °C in a high temperature furnace. All the plates were carbonized and then their DC electrical conductivity (σ_{DC}) was measured and is shown in Fig. 6A.

The conductivity (σ_{DC}) of GMCMS is 198.36 S cm^{-1}, which is quite high, the reason being that on heat treatment at higher temperature the defects in the layers decreases due to proper stacking of layers which leads to decrease in interlayer distance and further delocalization of π-electrons in the carbon network thereby forming a relatively more conducting network. The graphitized MCMS was further expanded by chemical treatment and conductivity of as such expanded MCMS was calculated to be 183.47 S cm^{-1} which is low as compared to GMCMS. This decrease in conductivity is due to the increase in *d*-spacing between graphitic layers which is already explained and discussed above.

When to above mentioned GMCMS and EMCMS, the Fe_3O_4 nanoparticles were added, a decrease in conductivity was observed as Fe_3O_4 acts as an inhibitor in the conduction path of the electrons. Addition of magnetic nanoparticles on the surface of MCMS increases the contact resistance and decreases the conductivity. Thus, Fe_3O_4 on being added to GMCMS and EMCMS reduces their conductivity to some extent. The (σ_{DC}) of Fe_3O_4 composite with GMCMS and EMCMB was found to be 185.02 S cm^{-1} and 169.98 S cm^{-1}, respectively. Additionally, on heat treatment at temperature above 650 °C carbon of the MCMS acts as a reducing agent and reacts with Fe_3O_4 to form FeC complex, which further reduces the conductivity of composites, although peak of FeC is not present in the XRD pattern.

Fig. 6B shows the total shielding effectiveness (SE_T) of GMCMS, EMCMS, GMCMS–Fe_3O_4 and EMCMS–Fe_3O_4 in the frequency range of 8.2 GHz to 12.4 GHz, whereas shielding effectiveness due to absorption (SE_A) and reflection (SE_R) for the same samples are presented in Fig. 6C and D, respectively. Generally, electromagnetic (EM) radiations reflect from conducting material and extent of reflection depends on the electrical conductivity and morphology of shield material. While, absorption of EM radiation can be controlled by magnetic and dielectric properties of shield materials. It is well known that the properties of MCMS can be tailored by its processing temperature because structure of carbon materials changes with heat treatment temperature.[35] As a consequence, electrical

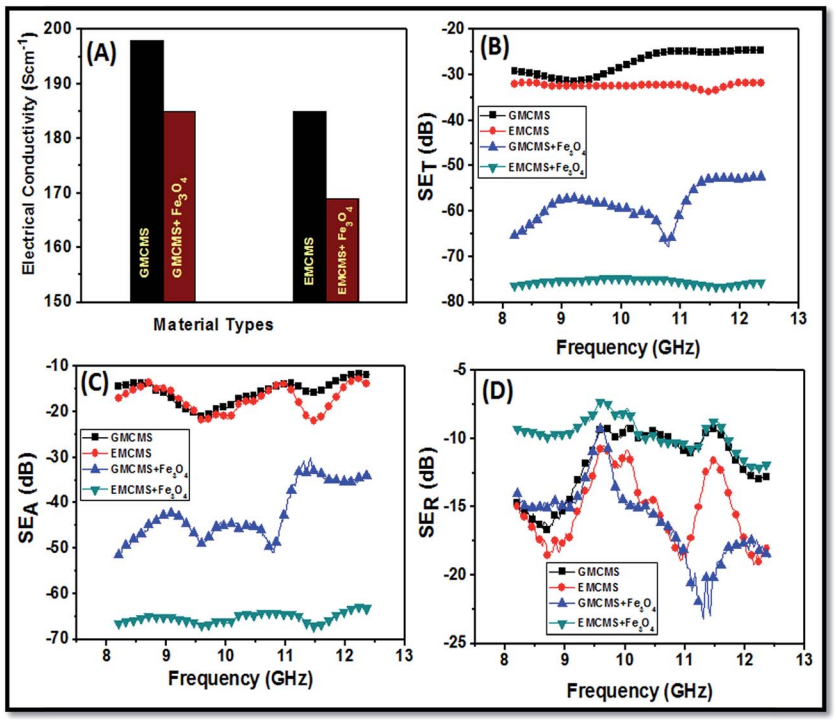

Fig. 6 DC electrical conductivity (A) of MCMS composites and (B–D) shielding effectiveness of MCMS composites in frequency range of 8.2 GHz to 12.4 GHz (a color version of this figure can be viewed online).

conductivity of carbon material increases with increasing temperature. In this investigation, GMCMS are heat treated to temperature 1400 °C and have quite high value of DC electrical conductivity (198.36 S cm^{-1}).

Suitability of MCMS as EMI shield can be elucidating by measuring SE in terms of reflection and absorption losses, as presented in Fig. 6C and D, respectively. The SE of a shield material is the ability to attenuate EM radiation that can be expressed in terms of ratio of incoming (incident) and outgoing (transmitted) power.[36] Higher values of SE in decibels (dB) signify less energy passes through the shield and most of the energy absorbed or reflected by shield material. EM attenuation offered by shield depends on the three mechanisms: reflection of the wave from the front face of shield, absorption of the wave as it passes through the shield and multiple reflections of the waves at various interfaces.[37] Therefore, total SE (SE_T) is attributed to three types of losses *viz.* reflection loss (SE_R), absorption loss (SE_A) and multiple reflection losses (SE_M) and it can be expressed as,

$$SE_T\ (dB) = SE_R + SE_A + SE_M = 10\log(P_t/P_i) \quad (1)$$

where, P_i and P_t are power of incident and transmitted EM waves respectively. As, the P_t is always less than P_i, therefore, SE_T is a negative quantity and more negative value means increase in magnitude of SE. It is significant to note that the losses associated with multiple reflections can be ignored ($SE_M \sim 0$) when SE of EMI shielding material is more than −10 dB (ref. 38) so that SE can be expressed as,

$$SE_T\ (dB) = SE_R + SE_A \quad (2)$$

It is observed from Fig. 6B that SE_T value for GMCMS and EMCMS is −29 and −32 dB, respectively, while in case of GMCMS–Fe_3O_4 and EMCMS–Fe_3O_4, it increased to −65.4 and −75.8 dB, respectively. It is interesting to note that SE_T of GMCMS–Fe_3O_4 and EMCMS–Fe_3O_4 is more than the double of GMCMS and EMCMS. In the case of GMCMS the SE_T is equally shared by reflection (14.7) and absorption (14.4) losses at frequency 8.2 GHz, while in case of EMCMS, the absorption loss SE_A (−17.0 dB) is slightly higher than SE_R (−15.0 dB) at frequency 8.2 GHz. On the other hand, SE_T in GMCMS–Fe_3O_4 and EMCMS–Fe_3O_4 is governed by absorption losses SE_A (−51.4 and −66.5 dB) and partially by reflection losses SE_R (−14 and −9.3 dB). SE_T (−75.8 dB) obtained for Fe_3O_4–EMCMS composite is much higher than the other new generation carbon materials, *i.e.* graphene, CNTs, carbon nanofibers *etc.* based Fe_3O_4–carbon composites. A comparison of results of Fe_3O_4–carbon based composites on the basis of previous literature is presented in Table 2. It is clearly observed from the literature that the outstanding SE_T (−75.8 dB) is obtained for MCMS based Fe_3O_4–EMCMS composite which was developed from very low cost pitches.

In GMCMS–Fe_3O_4 based shield material presence of ferrites nanoparticles improves the absorption losses which provide higher surface area and large interfacial area. On the other hand, excellent shielding effectiveness obtained in EMCMS–Fe_3O_4 composite is due to the combined effect of magnetic properties of Fe_3O_4 and higher BET surface area which helps in absorbing electromagnetic radiation.

4.4. Permittivity and magnetic permeability of MCMS composites

Further understand the mechanism in improvement of absorption of EM radiation by MCMS based different composites, EM parameters, *i.e.*, relative complex permittivity ($\varepsilon^* = \varepsilon' - i\varepsilon''$) and relative complex permeability ($\mu^* = \mu' - i\mu''$) have been measured in the frequency region of 8.2–12.4 GHz and are depicted in Fig. 7A and B. These complex parameters have been estimated from experimental scattering parameters (S_{11} & S_{21}) by standard Nicholson and Ross theoretical calculation.[50,51] The estimated real parts of the EM parameters (ε', μ') are directly associated with the amount of polarization occurring in the material and has storage ability of the electric and magnetic energy, while the imaginary parts (ε'', μ'') stand for electric and magnetic energy loss parts due relaxation phenomena of dipoles resulting in dissipation of EM energy as heat.

The complex values of permittivity and permeability typically correspond to attenuation in a medium in which real permittivity and permeability is related to wave propagation rather than attenuation. Fig. 7A and B clearly demonstrate real and imaginary part of the permittivity (ε', ε'') varying with frequency in X band for all MCMS composites. Real part of permittivity in GMCMS and EMCMS exhibits broad peaks in the frequency region 9.2–10.5 GHz and 11.6–12.4 GHz, respectively which reveals the resonance behaviour due to the high value of electrical conductivity (Fig. 6A). Furthermore, skin effect becomes significant in GMCMS composites due to its high surface area and high value of conductivity. While, ε' decreases with increasing the frequency in MCMS–Fe_3O_4 and EMCMS–Fe_3O_4. Decrease in permittivity in samples having Fe_3O_4 nanoparticles with frequency could be ascribed to the decreasing capability of the dipoles to sustain the in-phase movement with speedily pulsating electric vector of the incident radiation. The real permittivity at fixed frequency 10 GHz is 89, 56.5, 39.8 and 32.3 for GMCMS, EMCMS, GMCMS–Fe_3O_4 and EMCMS–Fe_3O_4 composites, respectively. However, in case of GMCMS–Fe_3O_4 and EMCMS–Fe_3O_4 composites due to the lower value of conductivity, interfacial polarization effect is comparatively small and as a result lowers the value of real permittivity. Therefore, impedance is much closer to impedance of free space due to lower value of real permittivity and hence, minimizing reflectivity. Thus, it becomes highly capable of absorbing EM radiation rather than reflection and also supports our results.

By incorporating Fe_3O_4 nanoparticles in GMCMS and EMCMS, electrical conductivity decreased in GMCMS–Fe_3O_4 and EMCMS–Fe_3O_4 composites leading to reduction in imaginary permittivity as shown in Fig. 7B. Reduction in imaginary permittivity is due the decrease in electrical conductivity according to eqn (3), which results in decrease in dielectric loss which is a ratio of imaginary to real part of permittivity ($\varepsilon''/\varepsilon'$).

Table 2 Electromagnetic interference shielding effectiveness of different samples reported in literature[a]

Samples	Thickness of sample (mm)	Frequency (GHz)	EMI shielding effectiveness (dB)
Carbon foam–Fe_3O_4–ZnO[20]	1.5	8.2–12.4	−48.5
RGO–γ-Fe_2O_3–carbon fiber composite[39]	0.2–0.4	8.2–12.4	−45.26
γ-Fe_2O_3–ordered mesoporous carbon[40]	1.6	11.2	−32 (RL)
Free standing Fe_3O_4–graphene nanosheet[41]	0.30	8.2–12.4	−22
MWCNT–Fe_3O_4 in PC/SAN blends[42]	—	18	−32.5
PS–reduced graphene oxide–Fe_3O_4 composite[43]	—	9.8–12	−30
CNTs–Fe_3O_4–PANI nanocomposites[44]	2.0	12.9	−48 (RL)
TiO_2 coated MWCNT–Fe_3O_4 (ref. 45)	2.0	10.98	−42.53 (RL)
Carbon nanofiber–Fe_3O_4 composite[46]	0.70	10.4	−67.90
RGO–Fe_3O_4 (ref. 47)	3.0	8.2–12.4	−41
Polyetherimide/graphene@Fe_3O_4 composite foams[48]	2.5	8–12	14.3–18.2
Fe_3O_4/Al_2O_3/carbon nanocoils[49]	3.1	8.2–12.4	−40.3 (RL)
EMCMS–Fe_3O_4 composite (present study)	2.5	8.2–12.4	−75.80

[a] ZnO (zinc oxide), RGO (reduced graphene oxide), MWCNT (multiwall carbon nanotubes), PC (polycarbonate), SAN [poly(styrene-*co*-acrylonitrile)], polystyrene (PS), PANI (polyaniline), Al_2O_3 (aluminium oxide).

Imaginary part of complex permittivity (ε'') is correlated with electrical conductivity, according to imaginary part formula as follows:

$$\varepsilon'' = \frac{\sigma_{DC}}{\omega\varepsilon_o} + \sigma_{AC} \quad (3)$$

The imaginary part ε'' is influenced by σ_{DC} and σ_{AC}.

Fig. 7A and B show real and imaginary parts of permeability (μ' and μ'') for all four samples. It can be seen that without Fe_3O_4 nanoparticles, the values of μ' and μ'' with frequency is ~0.2 and almost zero, respectively, therefore it confirms that GMCMS and EMCMS have no magnetic loss and microwave shielding effectiveness is dominated by dielectric loss only. However, composites with Fe_3O_4 nanoparticles exhibited much higher μ' and μ'' as compared to GMCMS and EMCMS composites. It indicates that microwave absorption in these samples is due to the dielectric and magnetic losses resulting in high value of total electromagnetic loss. Thus, higher value of real permeability is responsible for the radiation absorption in GMCMS–Fe_3O_4 and EMCMS–Fe_3O_4 composites (Fig. 7B). In MCMS, the existence of interfaces between Fe_3O_4

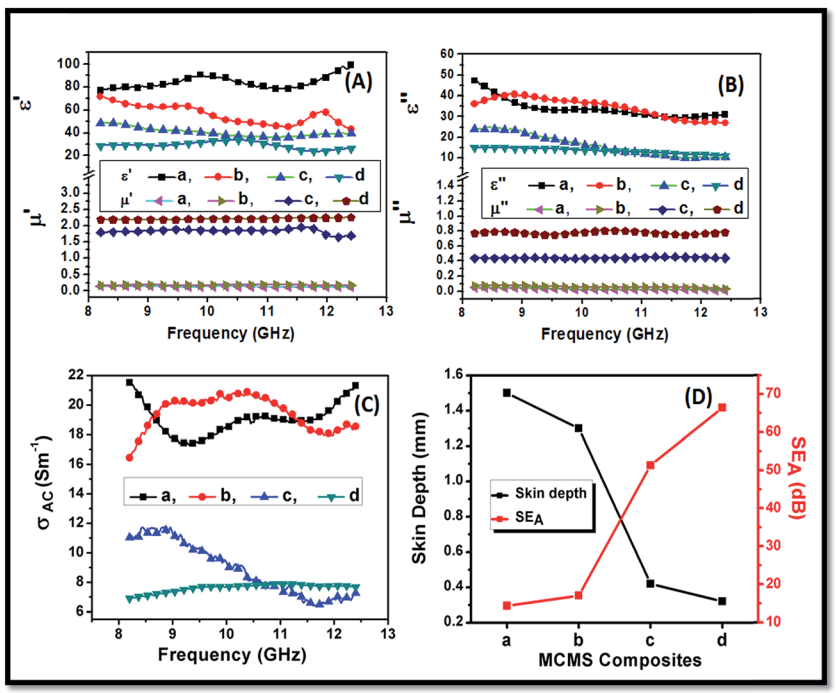

Fig. 7 The complex permittivity and permeability (A and B) of the MCMS composites (a = GMCMS, b = EMCMS, c = GMCMS–Fe_3O_4 and d = EMCMS–Fe_3O_4) (a color version of this figure can be viewed online).

nanoparticles–GMCMS and Fe_3O_4 nanoparticles–EMCMS are responsible for interfacial polarization[39] which further contribute to dielectric losses. Interfacial polarization occurs in heterogeneous media due to the accumulation of charges at the interfaces and the formation of large dipoles. Ferromagnetic nanoparticles also act as small dipoles which get polarized in the presence of EM field and facilitate the microwave absorption. In the microwave ranges, the natural resonances in the X-band can be attributed to the small size of Fe_3O_4 nanoparticles in the MCMS composites.

Fig. 7C shows frequency dependent AC electrical conductivity (σ_{AC}) for GMCMS, EMCMS, GMCMS–Fe_3O_4 and EMCMS–Fe_3O_4 composites. The value of σ_{AC} was calculated from the dielectric measurements by using formula $\sigma_{AC} = \omega\varepsilon_o\varepsilon''$, where, ω is equal to $2\pi f$, ε_o is the permittivity of the free space, and ε'' is imaginary part of permittivity. As observed, the change in σ_{AC} with frequency is irregular for all samples. It varies from 18–22 S cm^{-1} in GMCMS, 16–20 S cm^{-1} in EMCMS, 6.5–11.5 S cm^{-1} in GMCMS–Fe_3O_4 and 6.8–8.0 S cm^{-1} EMCMS–Fe_3O_4 samples in the X-band. It is clear that the trend of σ_{AC} for all samples is on the same line as observed in DC electrical conductivity.

Skin depth (δ) and absorption loss (SE_A) at fixed frequency of 8.2 GHz for all four samples have been shown in Fig. 7D. From eqn (4) and (5) it is clear that μ' is directly proportional to SE_A and it is also inversely proportional to δ because thickness (t) of sample is kept constant, *i.e.*, 2.5 mm. Therefore, GMCMS has higher skin depth (δ) of 1.5 mm and exhibits minimum absorption loss of about 14.4 dB. On the other hand, EMCMS–Fe_3O_4 composite exhibits maximum absorption loss of 66.5 dB and has the minimum skin depth of 0.3 mm.

$$\delta = (2/\sigma\omega\mu')^{1/2} \quad (4)$$

$$SE_A\ (dB) = -8.68(t/\delta) = -8.68t(\sigma\omega\mu'/2)^{1/2} \quad (5)$$

5. Conclusion

In conclusion, MCMS–Fe_3O_4 composites have been successfully synthesized by incorporating magnetic nanoparticles of iron oxide (Fe_3O_4) with GMCMS powder. The electromagnetic properties and microwave absorption capabilities were further improved by chemical expansion of GMCMS and addition of Fe_3O_4 nanoparticles. The GMCMS–Fe_3O_4 and EMCMS–Fe_3O_4 composites show excellent shielding effectiveness in the frequency range 8.2 GHz to 12.4 GHz with excellent absorption dominated total shielding effectiveness value of −65.4 (−51.4 dB absorption losses) in case of GMCMS–Fe_3O_4 and −75.8 (−66.5 dB absorption losses) in EMCMS–Fe_3O_4 composite. The maximum complex permeability is higher in case of EMCMS–Fe_3O_4 as compared to other composites. This shows that the outstanding total electromagnetic shielding effectiveness of EMCMS–Fe_3O_4 is due to the dielectric and magnetic losses of the material. The present results show that the as prepared magnetic nanoparticles–carbon composites can be used as highly effective microwave absorbing materials, and their ability to absorb microwaves can be attuned by introducing different magnetic nanoparticles. We have discovered a new method to obtain the outstanding microwave absorbing carbon–magnetic composites from an inexpensive coal tar pitch material.

Acknowledgements

Authors are highly grateful to the Director, CSIR-NPL, for his kind permission to publish the results. Authors wish to thank Dr Avanish Pratap Singh, Polymeric & Soft Materials Section for measurement of EMI shielding. Authors are thankful to Dr R. K. Kotnala and Dr R. P. Pant for their valuable help in magnetic properties measurement and XRD studies, respectively. Thanks are also due to Mr Jay Tavale for his SEM characterization. The authors express their sincere thanks to Dr Chandra Shekher, Director, CSIR-CEERI, Pilani for giving us an opportunity to cooperate in the network project sponsored by Council of Scientific and Industrial Research (CSIR).

References

1 Y. Qing, W. Zhou, F. Luo and D. Zhu, *J. Magn. Magn. Mater.*, 2009, **321**, 25–28.
2 N. Li, Y. Huang, F. Du, X. He, X. Lin, H. Gao, Y. Ma, F. Li, Y. Chen and P. C. Eklund, *Nano Lett.*, 2006, **6**, 1141–1145.
3 X. C. Tong, *Advanced materials and design for electromagnetic interference shielding*, CRC Press, 2008.
4 Y. Yang, M. C. Gupta, K. L. Dudley and R. W. Lawrence, *J. Nanosci. Nanotechnol.*, 2005, **5**, 927–931.
5 D. Bjorklof, *Compliance Engineer*, 1998, **15**, 10.
6 H. W. Markstein, *Electron Packaging Proceeding*, 1995, **35**, 4.
7 P. O'shen, *Evaluation Engineering*, 1998, **37**(6), 40–45.
8 D. Chung, *Carbon*, 2001, **39**, 279–285.
9 S. S. Azim, A. Satheesh, K. Ramu, S. Ramu and G. Venkatachari, *Prog. Org. Coat.*, 2006, **55**, 1–4.
10 T. K. Gupta, B. P. Singh, V. N. Singh, S. Teotia, A. P. Singh, I. Elizabeth, S. R. Dhakate, S. Dhawan and R. Mathur, *J. Mater. Chem. A*, 2014, **2**, 4256–4263.
11 D. Chung, *Carbon*, 2012, **50**, 3342–3353.
12 D. Chung, *J. Mater. Eng. Perform.*, 2000, **9**, 350–354.
13 X. Li, H. Yi, J. Zhang, J. Feng, F. Li, D. Xue, H. Zhang, Y. Peng and N. J. Mellors, *J. Nanopart. Res.*, 2013, **15**, 1–11.
14 L. Li, P. Yih and D. Chung, *J. Electron. Mater.*, 1992, **21**, 1065–1071.
15 V. Panwar, B. Kang, J.-O. Park, S. Park and R. Mehra, *Eur. Polym. J.*, 2009, **45**, 1777–1784.
16 S. Teotia, B. P. Singh, I. Elizabeth, V. N. Singh, R. Ravikumar, A. P. Singh, S. Gopukumar, S. K. Dhawan, A. Srivastava and R. B. Mathur, *RSC Adv.*, 2014, **4**, 33168–33174.
17 S. Kumari, A. Kumar, A. P. Singh, M. Garg, P. K. Dutta, S. K. Dhawan and R. B. Mathur, *RSC Adv.*, 2014, **4**, 23202–23209.
18 K. Singh, A. Ohlan, V. H. Pham, R. Balasubramaniyan, S. Varshney, J. Jang, S. H. Hur, W. M. Choi, M. Kumar and S. Dhawan, *Nanoscale*, 2013, **5**, 2411–2420.

19 Z. Chen, C. Xu, C. Ma, W. Ren and H. M. Cheng, *Adv. Mater.*, 2013, **25**, 1296–1300.
20 R. Kumar, A. P. Singh, M. Chand, R. P. Pant, R. K. Kotnala, S. K. Dhawan, R. B. Mathur and S. R. Dhakate, *RSC Adv.*, 2014, **4**, 23476–23484.
21 X. Luo and D. Chung, *Composites, Part B*, 1999, **30**, 227–231.
22 S. Yang, K. Lozano, A. Lomeli, H. D. Foltz and R. Jones, *Composites, Part A*, 2005, **36**, 691–697.
23 S. Hossain, Y.-K. Kim, Y. Saleh and R. Loutfy, *J. Power Sources*, 2003, **114**, 264–276.
24 G. Wang, J. Yao and H. Liu, *Electrochem. Solid-State Lett.*, 2004, **7**, A250–A253.
25 F. M. Courtel, S. Niketic, D. Duguay, Y. Abu-Lebdeh and I. J. Davidson, *J. Power Sources*, 2011, **196**, 2128–2134.
26 K. Singh, A. Ohlan, P. Saini and S. Dhawan, *Polym. Adv. Technol.*, 2008, **19**, 229–236.
27 X. Sun, J. He, G. Li, J. Tang, T. Wang, Y. Guo and H. Xue, *J. Mater. Chem. C*, 2013, **1**, 765–777.
28 C. Liang, C. Liu, H. Wang, L. Wu, Z. Jiang, Y. Xu, B. Shen and Z. Wang, *J. Mater. Chem. A*, 2014, **2**, 16397–16402.
29 Z. Wang, L. Wu, J. Zhou, Z. Jiang and B. Shen, *Nanoscale*, 2014, **6**, 12298–12302.
30 Z. Wang, L. Wu, J. Zhou, B. Shen and Z. Jiang, *RSC Adv.*, 2013, **3**, 3309–3315.
31 D. C. Marcano, D. V. Kosynkin, J. M. Berlin, A. Sinitskii, Z. Sun, A. Slesarev, L. B. Alemany, W. Lu and J. M. Tour, *ACS Nano*, 2010, **4**, 4806–4814.
32 H. Itoh and T. Sugimoto, *J. Colloid Interface Sci.*, 2003, **265**, 283–295.
33 W. Voit, D. Kim, W. Zapka, M. Muhammed and K. Rao, *MRS Proceedings*, 2002, 676.
34 S. Dhakate, P. Bahl and P. Sahare, *J. Mater. Sci. Lett.*, 2000, **19**, 1959–1961.
35 S. Dhakate and O. Bahl, *Carbon*, 2003, **41**, 1193–1203.
36 D.-X. Yan, P.-G. Ren, H. Pang, Q. Fu, M.-B. Yang and Z.-M. Li, *J. Mater. Chem.*, 2012, **22**, 18772–18774.
37 R. Kumar, S. R. Dhakate, P. Saini and R. B. Mathur, *RSC Adv.*, 2013, **3**, 4145–4151.
38 X. Han and Y. Wang, *J. Funct. Mater. Devices*, 2007, **13**, 529.
39 A. P. Singh, P. Garg, F. Alam, K. Singh, R. Mathur, R. Tandon, A. Chandra and S. Dhawan, *Carbon*, 2012, **50**, 3868–3875.
40 J. Wang, H. Zhou, J. Zhuang and Q. Liu, *Phys. Chem. Chem. Phys.*, 2015, **17**, 3802–3812.
41 W.-L. Song, X.-T. Guan, L.-Z. Fan, W.-Q. Cao, C.-Y. Wang, Q.-L. Zhao and M.-S. Cao, *J. Mater. Chem. A*, 2015, **3**, 2097–2107.
42 S. P. Pawar, D. A. Marathe, K. Pattabhi and S. Bose, *J. Mater. Chem. A*, 2015, **3**, 656–669.
43 Y. Chen, Y. Wang, H.-B. Zhang, X. Li, C.-X. Gui and Z.-Z. Yu, *Carbon*, 2015, **82**, 67–76.
44 D. Zhang, X. Yang, J. Cheng, M. Lu, B. Zhao and M. Cao, *J. Nanomater.*, 2013, **2013**, 134.
45 P. Bhattacharya, S. Sahoo and C. Das, *eXPRESS Polym. Lett.*, 2013, **7**, 212–223.
46 M. Bayat, H. Yang, F. Ko, D. Michelson and A. Mei, *Polymer*, 2014, **55**, 936–943.
47 M. Mishra, A. P. Singh, B. Singh, V. Singh and S. Dhawan, *J. Mater. Chem. A*, 2014, **2**, 13159–13168.
48 B. Shen, W. Zhai, M. Tao, J. Ling and W. Zheng, *ACS Appl. Mater. Interfaces*, 2013, **5**, 11383–11391.
49 X. Qi, J. Xu, W. Zhong and Y. Du, *Diamond Relat. Mater.*, 2015, **51**, 30–33.
50 R. Kumar, S. R. Dhakate, T. Gupta, P. Saini, B. P. Singh and R. B. Mathur, *J. Mater. Chem. A*, 2013, **1**, 5727–5735.
51 A. Nicolson and G. Ross, *IEEE Trans. Instrum. Meas.*, 1970, **19**, 377–382.